Supplementary Material For:

Quasi-static Deformation Simulations of Molecular Crystals

NB Movies referred to below are provided as separate movie files

Mustafa S. Hamad[a], Catherine Boissier[b], Victor M. Calo[c], Julian D. Gale[a], Sten O. Nilsson Lill[d], Gordon M. Parkinson[e], Andrew L. Rohl[f]*

[a]*Curtin Institute for Computation and School of Molecular and Life Sciences, Curtin University, P.O. Box U1987, Perth, WA 6845, Australia.*

[b]*Oral Product Development, Pharmaceutical Technology & Development, Operations, AstraZeneca Gothenburg, SE-431 83, Mölndal, Sweden.*

[c]*School of Electrical Engineering, Computing and Mathematical Sciences, Curtin University, P.O. Box U1987, Perth, WA 6845, Australia.*

[d]*Data Science & Modelling, Pharmaceutical Sciences, R&D, AstraZeneca Gothenburg, SE-431 83, Mölndal, Sweden.*

[e]*Curtin University of Technology, Office of Research and Development, P. O. Box 1987, Perth, WA 6845, Australia.*

[f]*Curtin Institute for Computation and School of Electrical Engineering, Computing and Mathematical Sciences, Curtin University, P.O. Box U1987, Perth, WA 6845, Australia.*

**Corresponding Author: andrew.rohl@curtin.edu.au*

S1: Force Field and Cell Representations of β-Oxygen:

The form of the force field comprises a 12-6 Lennard-Jones potential to model non-bonded interactions and a harmonic potential to model the bonded interactions between two oxygen atoms. Following [1], the force constant of the harmonic interaction is set to 71 eV/Å^2 to reproduce the observed intramolecular vibrational frequency of 1552.5 cm^{-1}. A potential cut-off of 20 Å was used with a smooth tapering to zero over the last 3 Å via a Mei-Daveport-Fernando form [2]. Table S1.1 compares the calculated lattice parameters and other properties for β-oxygen with literature data and shows that the present implementation of Cheung's force field successfully reproduces these values.

Properties	Our Calculation	Literature Data	Reference
Lattice parameter, a_0 (Å)	3.3333	3.272	[1]
Lattice parameter, c_0 (Å)	10.771	11.277	[1]
Low frequency (cm^{-1})	46.46	51.00	[3]
High frequency (cm^{-1})	1555.25	1552.50	[3]

U_{static} (kJ/mol)	-9.35	-8.79	[1]
Density (kg/m^3)	1.538	1.530	[4]

Table S1.1: Comparison of the calculation properties of β-oxygen and those reported in the literature.

Figure S1.1 shows the unit cell of β-oxygen in rhombohedral (a) and hexagonal (b) forms. The (111) cell in Figure S1.1 (b) is very similar to the (111) cell in FCC metals, except molecules occupy lattice sites instead of atoms.

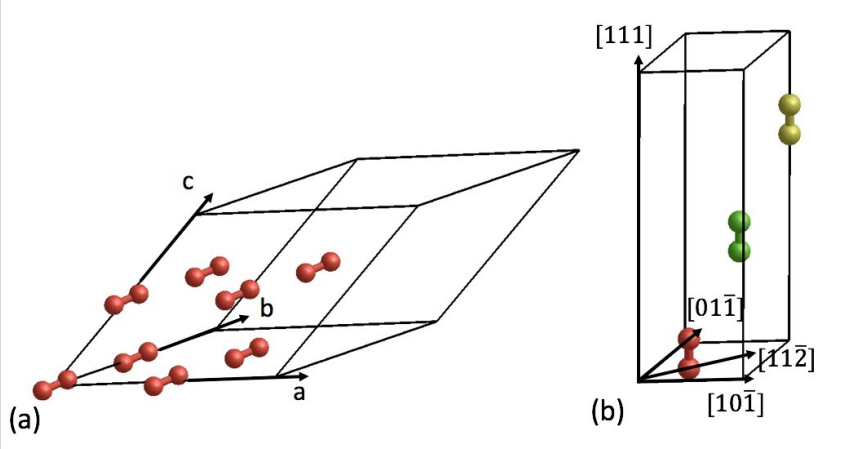

Figure S1.1: Unit cell of β-oxygen in either the (a) rhombohedral representation or (b) hexagonal form. Lattice vectors and directions are shown by the arrows. The red, green, and yellow oxygen molecules in (b) represent the ABC stacking motif in the (111) plane.

S2: Details of the Slip Systems Tested for β-Oxygen:

This work extensively deals with higher index planes and directions in β-oxygen. This leads to difficulty in mentally visualising the simulated geometry. In order to assist with this, this section of supplementary material provides illustrations and details on the crystallographic directions and planes of β-oxygen studied. The illustrations themselves represent surface cells and not supercells. Periodic images were added in the three Cartesian directions and the top view showing the slip systems looks down on the z-axis of the cell. All the calculations to find the higher index slip directions were carried out using a Python script and visualisations were made using the GDIS software [5].

Plane	(110)	(112)	(113)	(114)	(115)	(116)
Twin	[001]	[$\bar{1}$11]	[$\bar{3}\bar{3}$2]	[$\bar{2}\bar{2}$1]	[$\bar{5}\bar{5}$2]	[$\bar{3}\bar{3}$1]
Anti-twin	[00$\bar{1}$]	[11$\bar{1}$]	[33$\bar{2}$]	[22$\bar{1}$]	[55$\bar{2}$]	[33$\bar{1}$]
Diagonal	[$\bar{1}$10]	[1$\bar{1}$0]	[$\bar{1}$10]	[$\bar{1}$10]	[$\bar{1}$10]	[$\bar{1}$10]
135°	[$\bar{6}\bar{6}$5]	[13 $\bar{3}$ $\bar{5}$]	[$\bar{8}\bar{2}\bar{2}$]	[$\bar{6}\bar{2}$1]	[$\bar{7}\bar{2}$1]	[$\bar{3}\bar{9}$1]
45°	[$\bar{6}$65]	[3 $\bar{1}$3 5]	[$\bar{2}$82]	[$\bar{2}$61]	[$\bar{2}$71]	[$\bar{9}$31]
δ	61.8°	43°	56.2°	61.8°	64.9°	66.8°

Table S2.1: Summary of crystallographic directions (to within 3° for the "45°" and "135°" directions) and their corresponding notation. δ is the inclination angle, defined as the angle between the molecular vector and the z-axis.

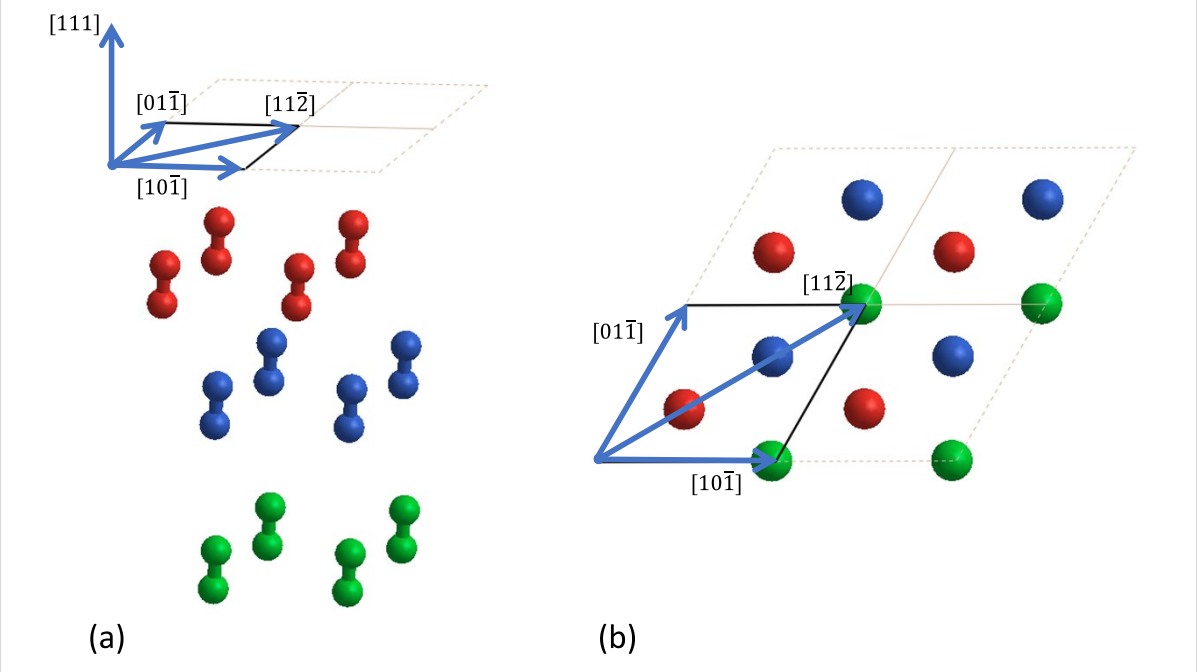

Figure S2.1: Schematic showing an example of the (111) surface cell in β-oxygen with the corresponding lattice directions in (a), and the top view of the same in (b). Note the ABC stacking (red, blue, green) characteristic of the {111}<11$\bar{2}$> in FCC structures.

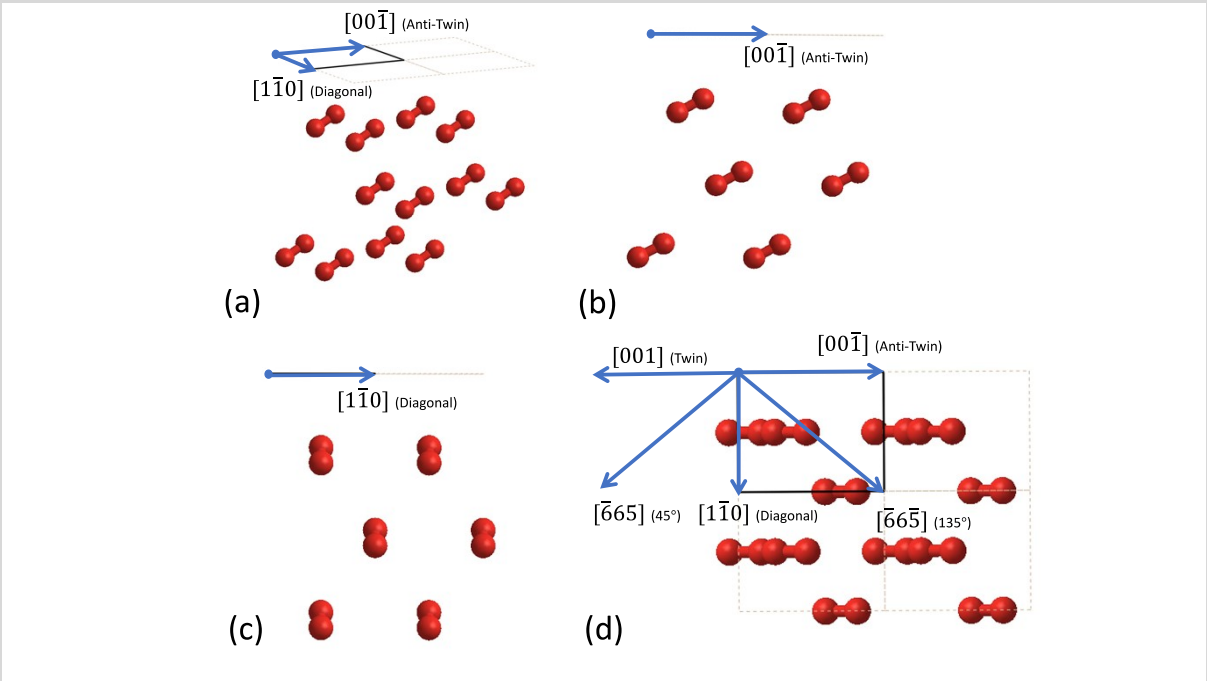

Figure S2.2: Schematic showing an example of the (110) surface cell in β-oxygen with the anti-twin and the diagonal directions indicated in (a), side view of the same structure in (a) shown in (b), another side view of the same structure in (a) shown in (c), top view of the structure in (a) with all the attempted slip systems indicated.

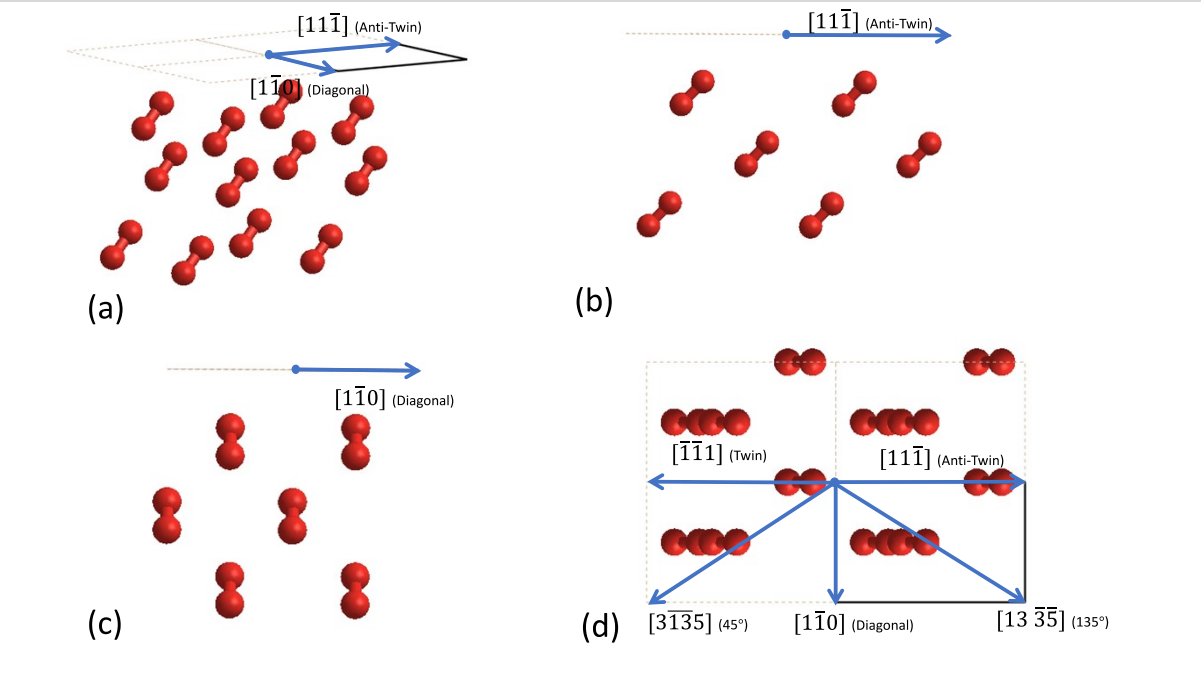

Figure S2.3: Schematic showing an example of the (112) surface cell in β-oxygen with the anti-twin and the diagonal directions indicated in (a), side view of the same structure in (a) shown in (b), another side view of the same structure in (a) shown in (c), top view of the structure in (a) with all the attempted slip systems indicated.

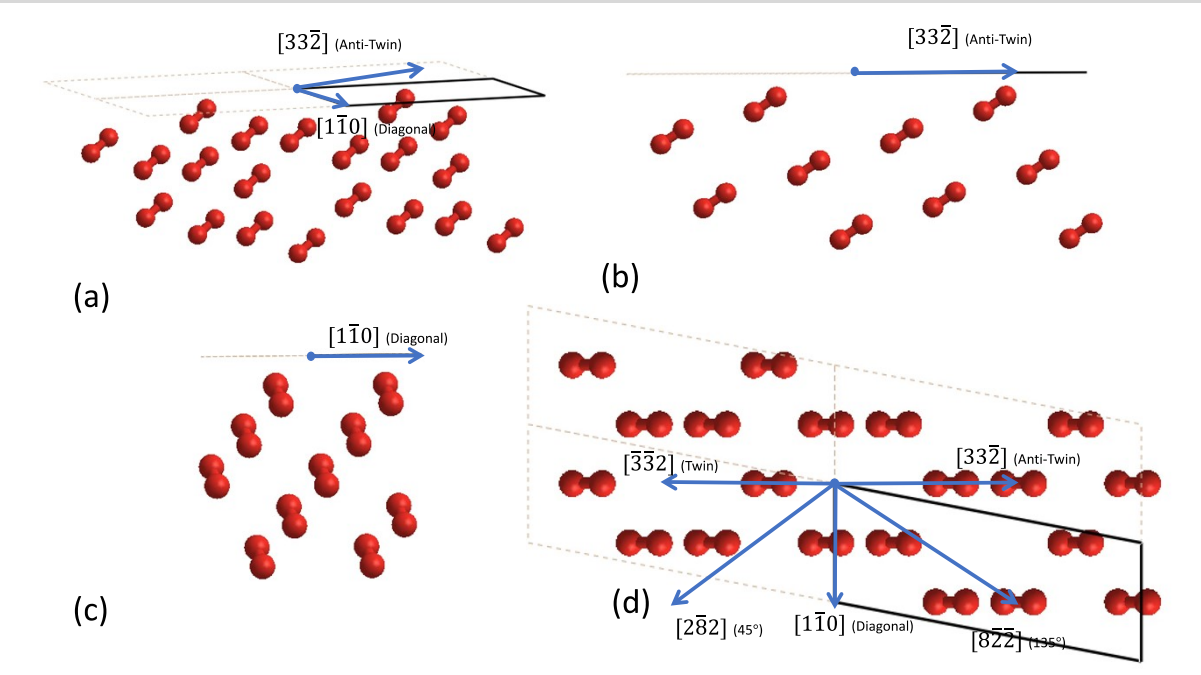

Figure S2.4: Schematic showing an example of the (113) surface cell in β-oxygen with the anti-twin and the diagonal directions indicated in (a), side view of the same structure in (a) shown in (b), another side view of the same structure in (a) shown in (c), top view of the structure in (a) with all the attempted slip systems indicated.

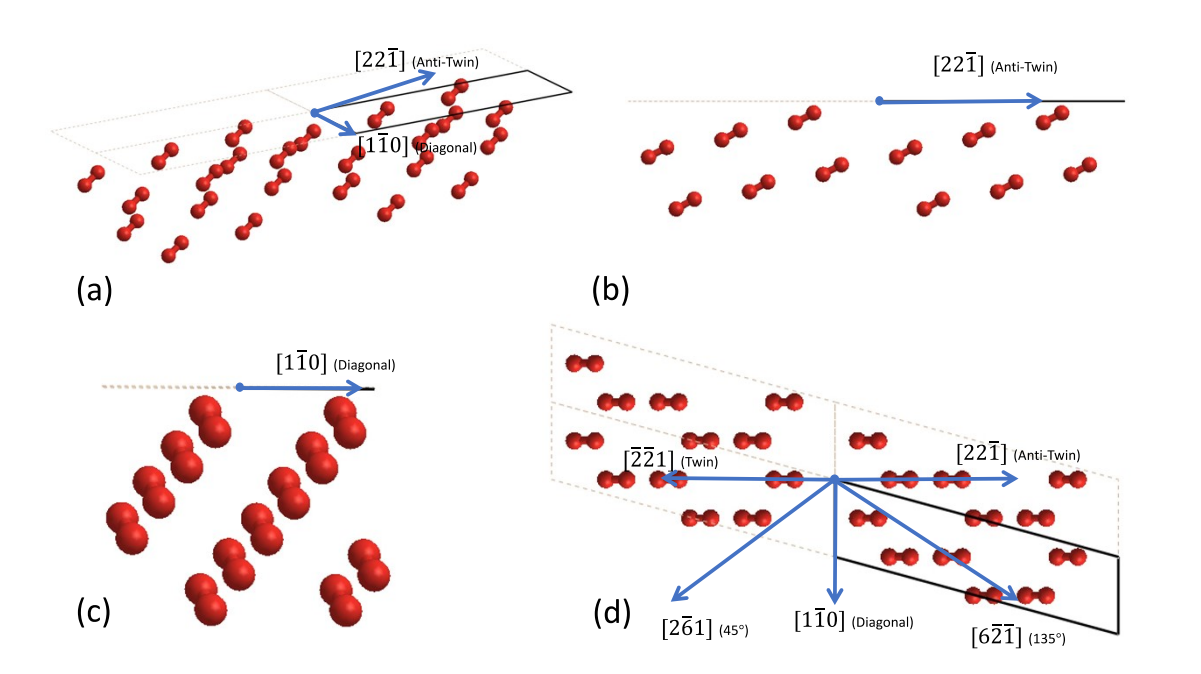

Figure S2.5: Schematic showing an example of the (114) surface cell in β-oxygen with the anti-twin and the diagonal directions indicated in (a), side view of the same structure in (a) shown in (b), another side view of the same structure in (a) shown in (c), top view of the structure in (a) with all the attempted slip systems indicated.

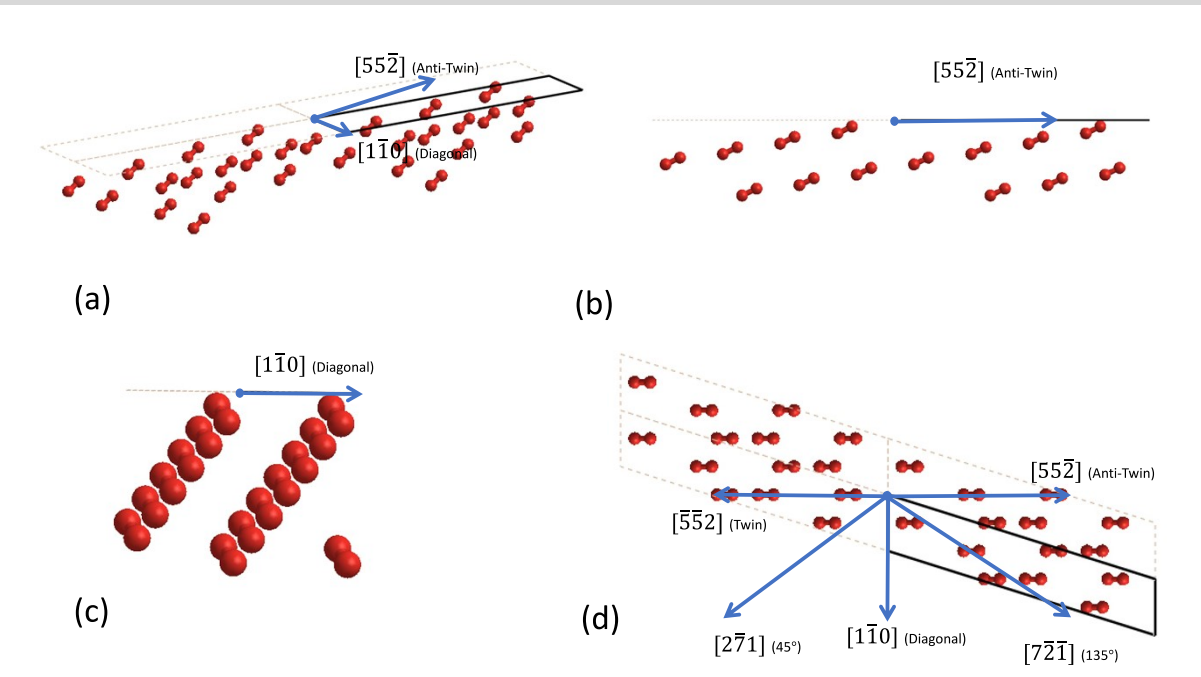

Figure S2.6: Schematic showing an example of the (115) surface cell in β-oxygen with the anti-twin and the diagonal directions indicated in (a), side view of the same structure in (a) shown in (b), another side view of the same structure in (a) shown in (c), top view of the structure in (a) with all the attempted slip systems indicated.

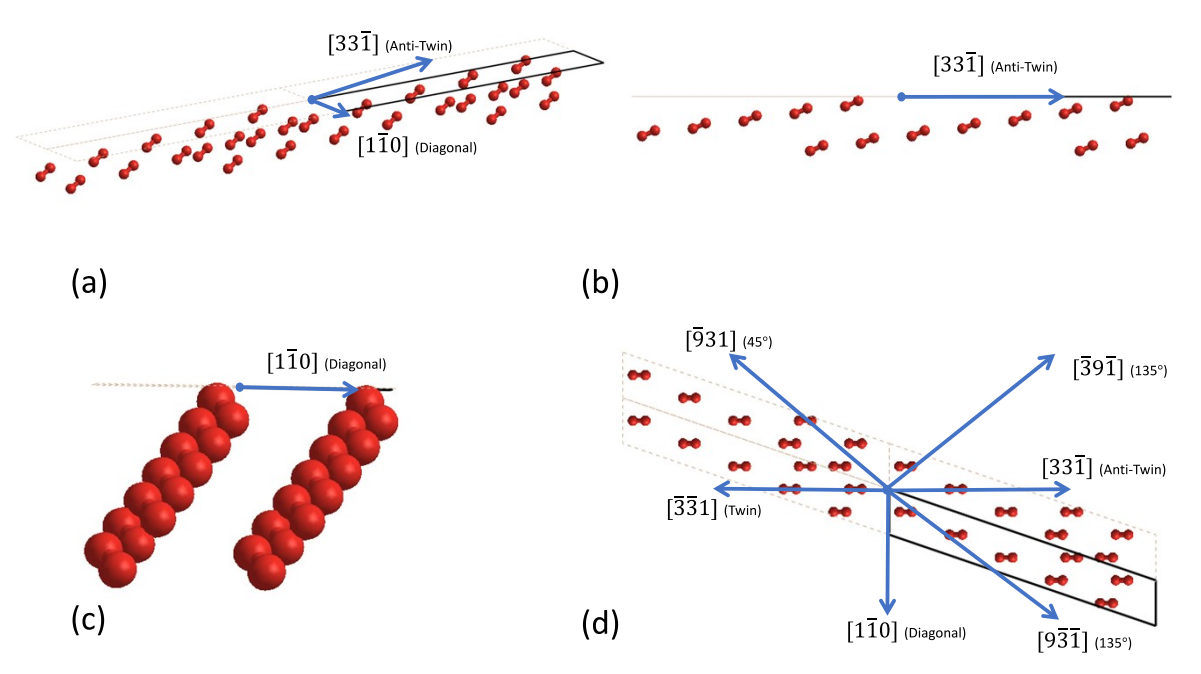

Figure S2.7: Schematic showing an example of the (116) surface cell in β-oxygen with the anti-twin and the diagonal directions indicated in (a), side view of the same structure in (a) shown in (b), another side view of the same structure in (a) shown in (c), top view of the structure in (a) with all the attempted slip systems indicated. For this plane, the [$\bar{3}9\bar{1}$] direction was chosen for deformation simulations while noting that it is symmetry equivalent to the [$9\bar{3}\bar{1}$] direction. The same applies to the [$\bar{9}31$] direction.

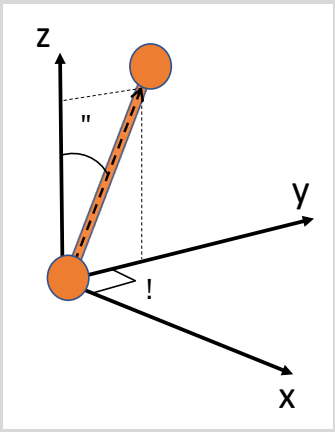

Figure S2.8: Schematic showing the inclination angle, δ, and azimuth angle, θ, of an oxygen molecule (or its molecular vector). The angles are defined with respect to the Cartesian axes not the crystallographic basis. Note that based on Figures S2.2 to Figures S2.7, the projection of the molecular vector onto the *xy* plane is always parallel, anti-parallel, and perpendicular, to the twin, anti-twin, and diagonal directions, respectively, implying that the definition of the angles is the same across the attempted slip systems.

S3: ESP Derived Partial Charges of Anthracene

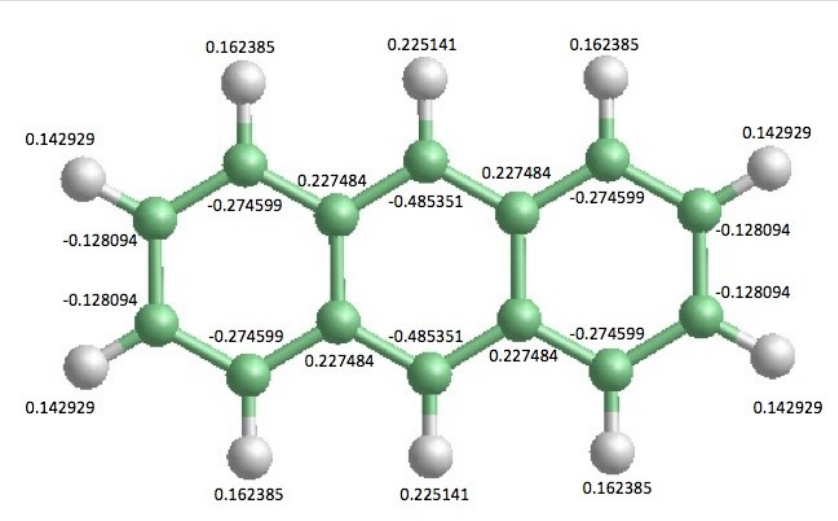

Figure S3.1: The ESP derived charges (a.u.) of carbon (green) and hydrogen (white) atoms of anthracene.

S4: Convergence Analysis for Oxygen and Anthracene

S4.1: RBSM

The main text identified two important convergence parameters in RBSM that need to be investigated. The first is the size of region one (i.e. number of molecules in region one), and the second is the number of shear steps for a converged system size. We set the size of each rigid block for oxygen and anthracene to be six and two layers, respectively, and then conduct extensive simulations as shown below while noting that the chosen sizes of the rigid blocks do converge the surface energies.

For oxygen, we performed RBSM shear simulations by varying the size of region one from one to 45 for (110)[00$\bar{1}$], (110)[001], (111)[10$\bar{1}$], and (111)[11$\bar{2}$], then recorded the slip barriers – U_N just before slip, as shown in Figure S4.1.1. Our results indicate that 12 layers in region 1 converges the barrier for all the slip systems tested.

Next, we took the twelve layer configurations for each slip system and performed strain step analysis by varying the strain step size from about 0.01 to 0.0001 strain per step, as shown in Figure S4.1.2. The barriers are converged for all slip systems for a strain step less than or equal to 0.0008 strain/step.

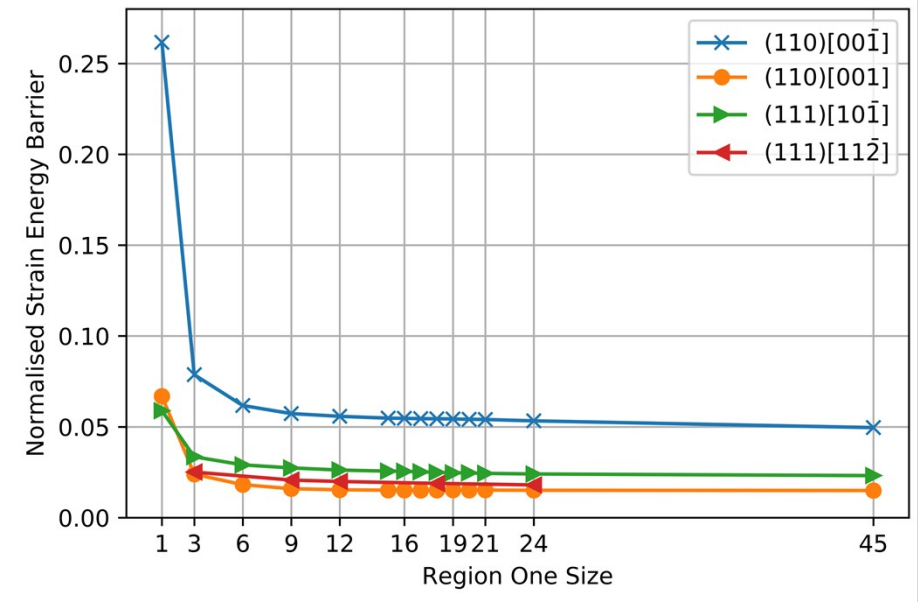

Figure S4.1.1: The RBSM normalised strain energy barriers of the first slip event as a function of the size of the system, across four different slip systems, as shown in the legend. The strain per step varied from 0.0003 to 0.0008 as the size of the system decreased. Lines are a guide to the eye only.

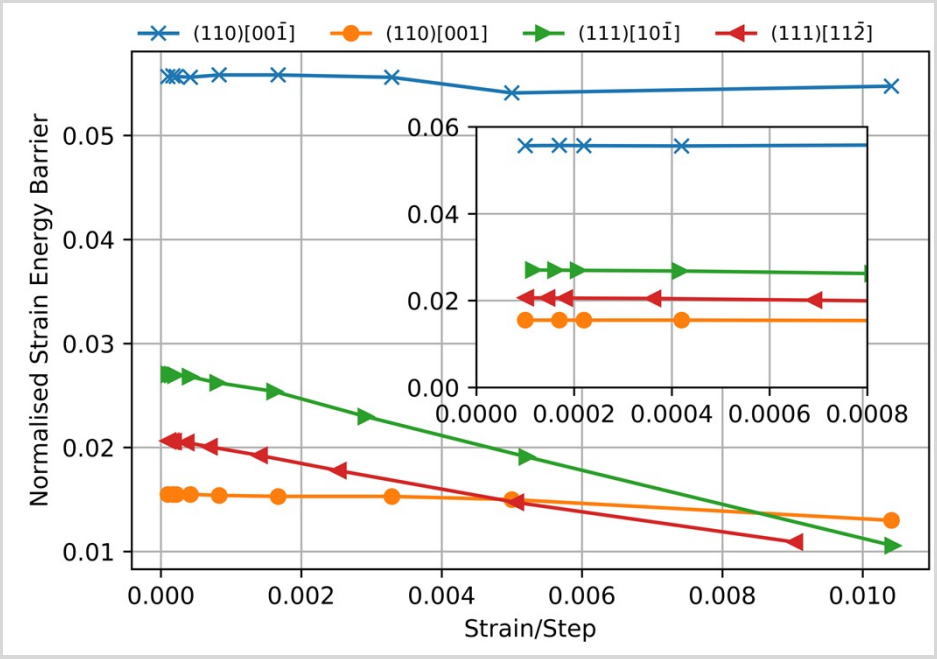

Figure S4.1.2: The RBSM normalised strain energy barriers of the first slip event as a function of the step size, across four different slip systems, as shown in the legend. The sizes of the systems were twelve layers each and the strain per step varied as shown on the *x*-axis. Inset plot shows the important barriers to demonstrate convergence at very small strain steps. Lines are a guide to the eye only.

RBSM convergence analysis was also conducted for shearing anthracene. For system size convergence tests of the (001)[100] case, the size of region one varied from 1 to 16, and the computed barriers are shown in Figure S4.1.3. It is evident that the barriers are converged for systems having 10 layers or more in region one.

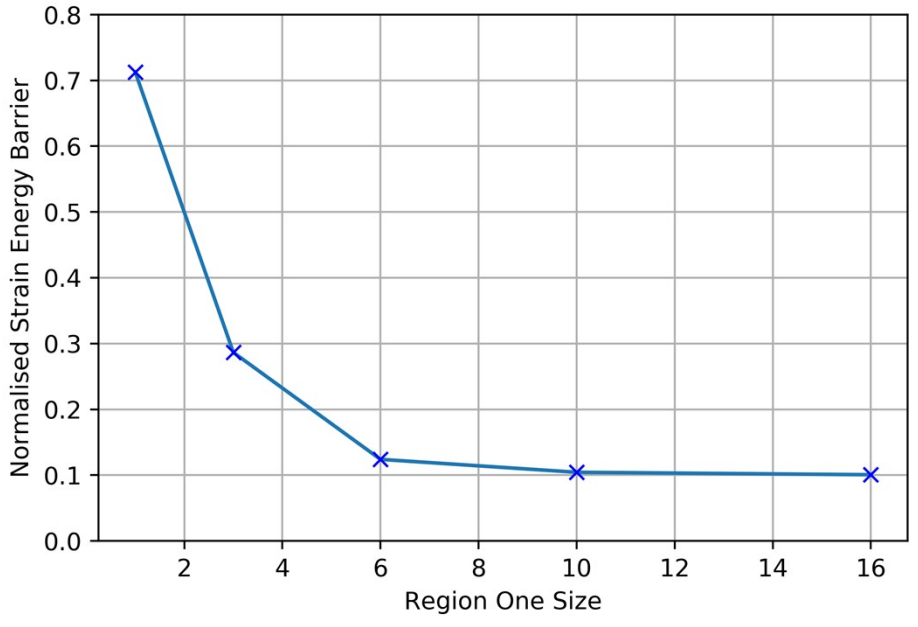

Figure S4.1.3: RBSM convergence analysis of the normalised strain energy barrier as a function of the size of the system for anthracene sheared in the (001)[100] slip system at 0.004 strain per step.

Shear step size analysis was conducted for the 10 layer system in (001)[100] by varying the strain step from 0.013 to 0.00014. The results in Figure S4.1.4 show that the barrier readily converges for a strain per step equal to or less than 0.008.

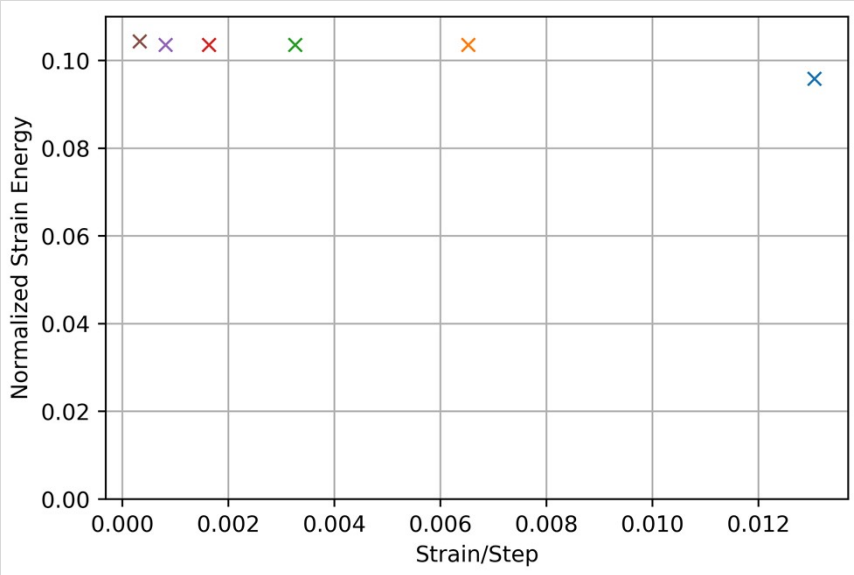

Figure S4.1.4: RBSM convergence analysis of the normalised strain energy barrier as a function of the strain step for the ten layer configuration of anthracene sheared in the (001)[100] slip system.

Although convergence analysis was conducted for selected slip systems, we assume that the converged parameters are equally applicable to the rest of the slip systems.

S4.2: TBSM

As in the case of RBSM, convergence of parameters needs to be inspected for TBSM. We start by testing the case of oxygen as shown in Figure S4.2.1. It is clear that the barrier converges

for system sizes equal to or greater than twelve for all four slip systems, and Figure S4.2.2 shows that the barriers approach convergence for a strain step equal to or less than 0.004.

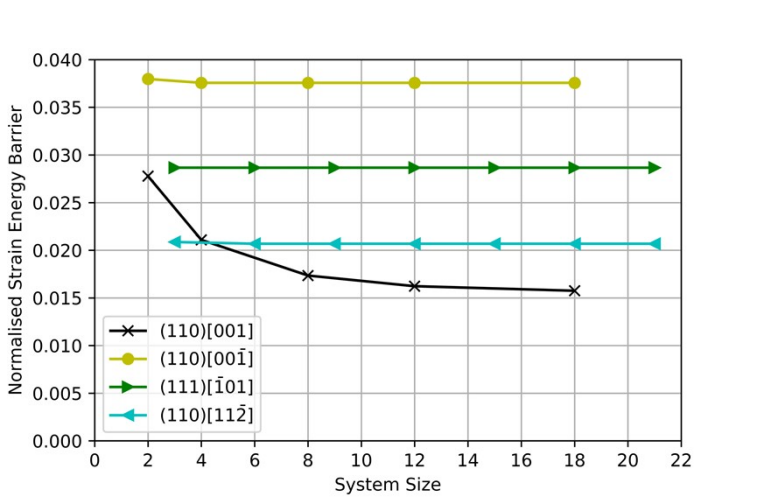

Figure S4.2.1: The TBSM normalised strain energy barriers of the first slip event as a function of the system size (number of layers in the supercell), across four different slip systems for oxygen, as shown in the legend. The strain step was set to 0.0008 for all simulations. Lines are a guide to the eye only.

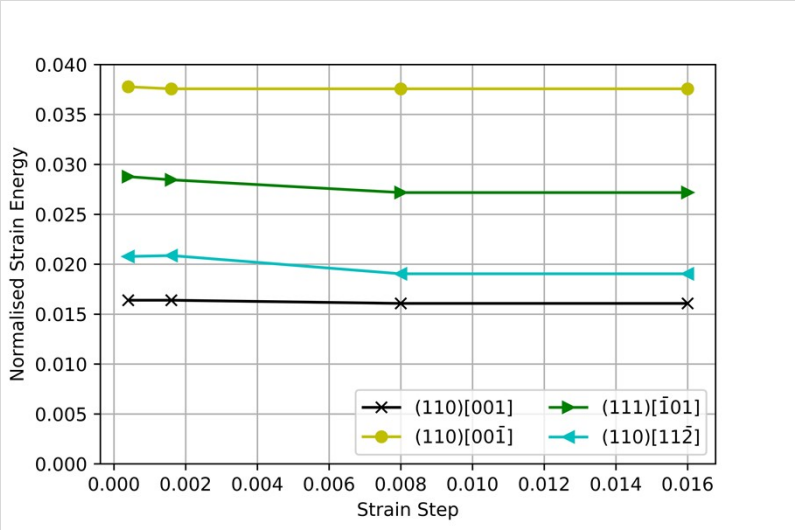

Figure S4.2.2: The TBSM normalised strain energy barriers of the first slip event as a function of the step size, across four different slip systems for oxygen, as shown in the legend. The system size was 12 layers for all simulations. Lines are a guide to the eye only.

TBSM convergence analysis was conducted for anthracene using (001)[100] by varying the supercell size from two to ten layers, showing that the normalised strain energy plot is insensitive to the system size. Investigation of the convergence of the barrier as a function of strain step, as shown in Figure S4.2.3, showed that the barrier converges for strain steps less than or equal to 0.01.

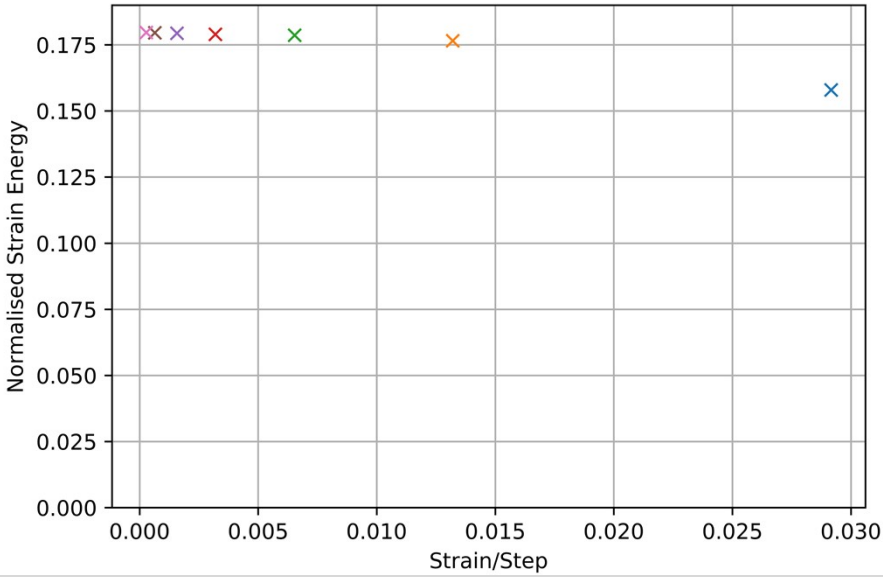

Figure S4.2.3: TBSM convergence analysis of the normalised strain energy barrier as a function of the strain step for the ten layer configuration of anthracene sheared in the (001)[100] slip system.

As in the case of RBSM, we conducted selected convergence analysis simulations and thereafter assume the converged parameters are equally applicable to the rest of the slip systems.

S5: Slip Movies of β-oxygen Deformation in (111)

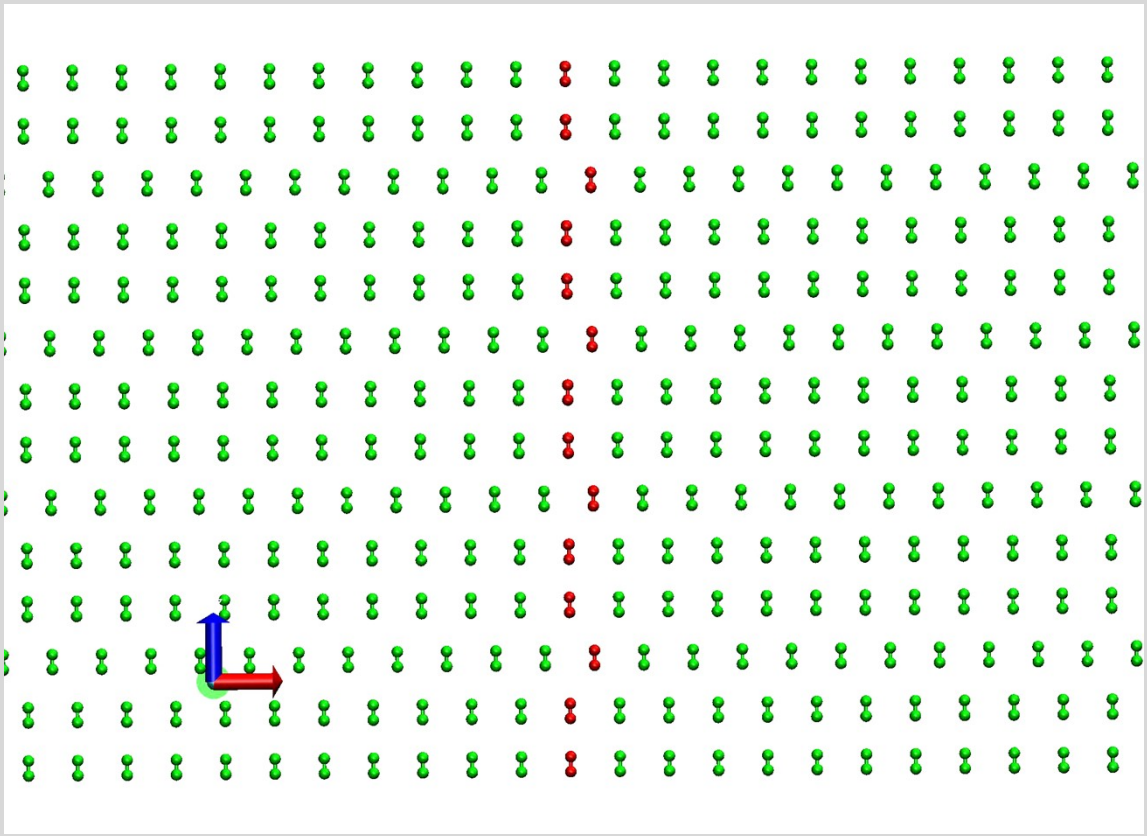

Movie S5.1: RBSM deformation movie of the 12 layer system sheared along (111)[$10\bar{1}$]. Green molecules represent periodic images of the reference structure, while red molecules represent the configuration throughout the deformation path. The top-most red molecule represents region three (the other five molecules are not

shown) and the bottom-most molecule represents the molecule in region two (again the other five molecules are not shown). The $[10\bar{1}]$ direction is aligned along x (red reference arrow) and [111] aligned along z (blue reference arrow). Changes in the inclination angle, δ, e.g. forward tilt of the molecules, are easily observed.

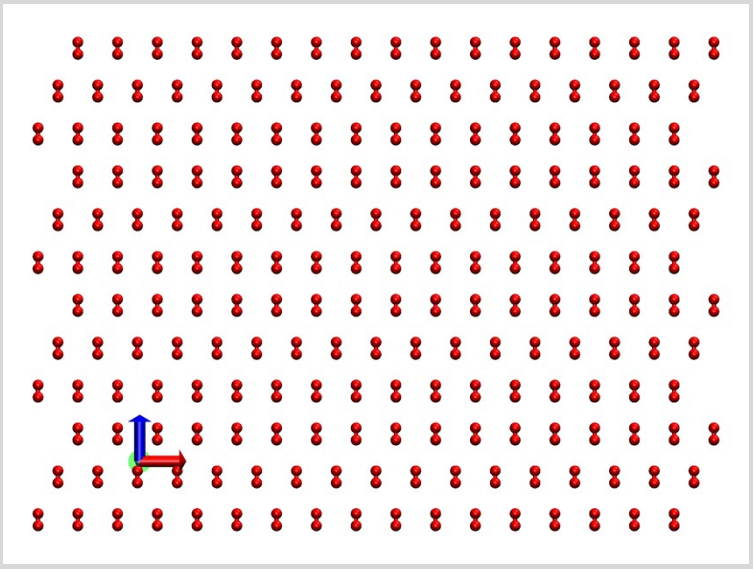

Movie S5.2: TBSM deformation movie of the 12 layer system sheared along (111)$[10\bar{1}]$. Periodic images of the supercell were produced along the x-axis. The $[10\bar{1}]$ direction is aligned along x (red reference arrow) and [111] aligned along z (blue reference arrow).

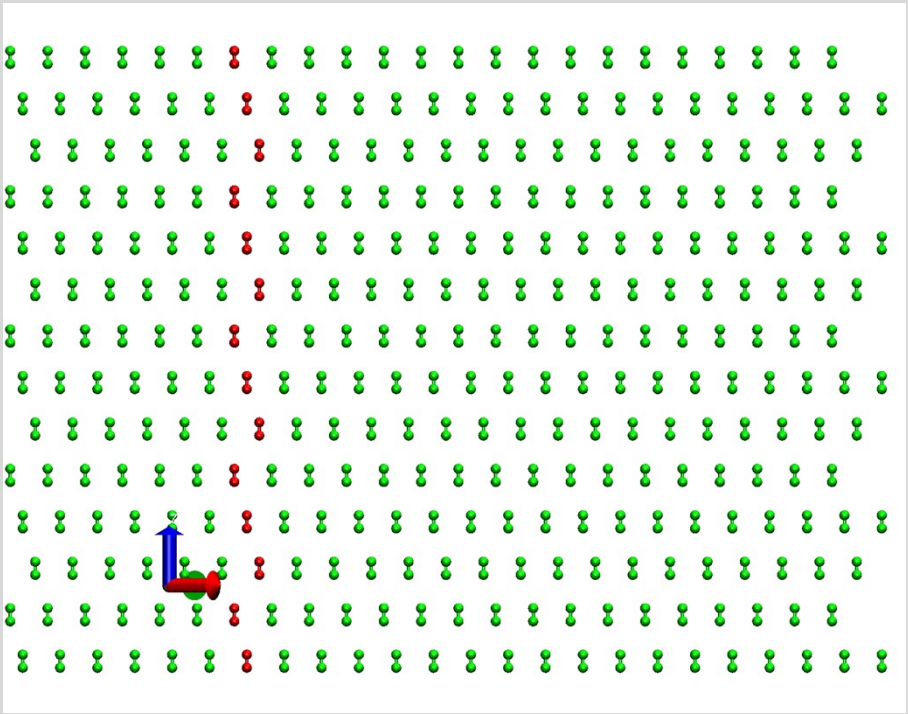

Movie S5.3: RBSM deformation movie of the 12 layer system sheared along (111)$[11\bar{2}]$. Green molecules represent periodic images of the reference structure, while red molecules represent the configuration throughout the deformation path. The top-most red molecule represents region three (the other five molecules are not shown) and the bottom-most molecule represents the molecule in region two (again the other five molecules are not shown). The $[11\bar{2}]$ direction is aligned parallel to the rows of molecules and [111] is aligned along z (blue reference arrow).

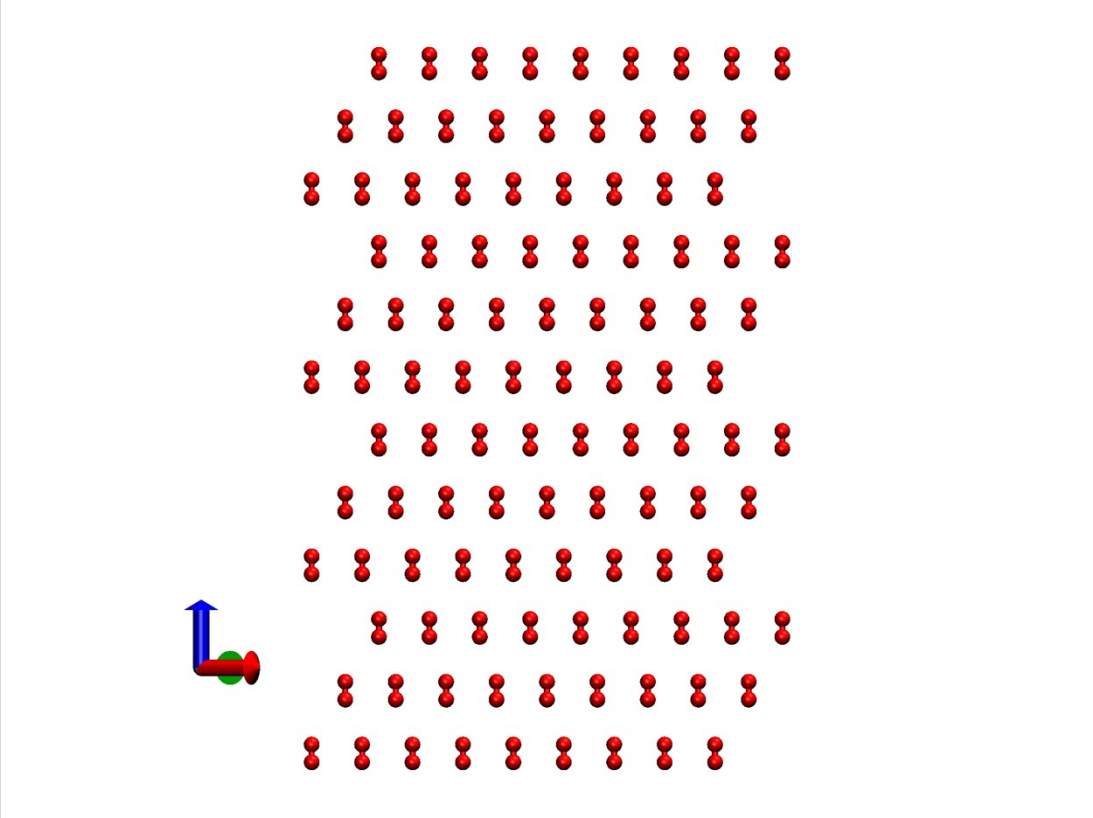

Movie S5.4: TBSM deformation movie of the 12 layer system sheared along (111)[$11\bar{2}$]. Periodic images of the supercell were produced along the *x*-axis *and y*-axis. The [$11\bar{2}$] direction is aligned parallel to the rows of the molecules and [111] is aligned along *z* (blue reference arrow).

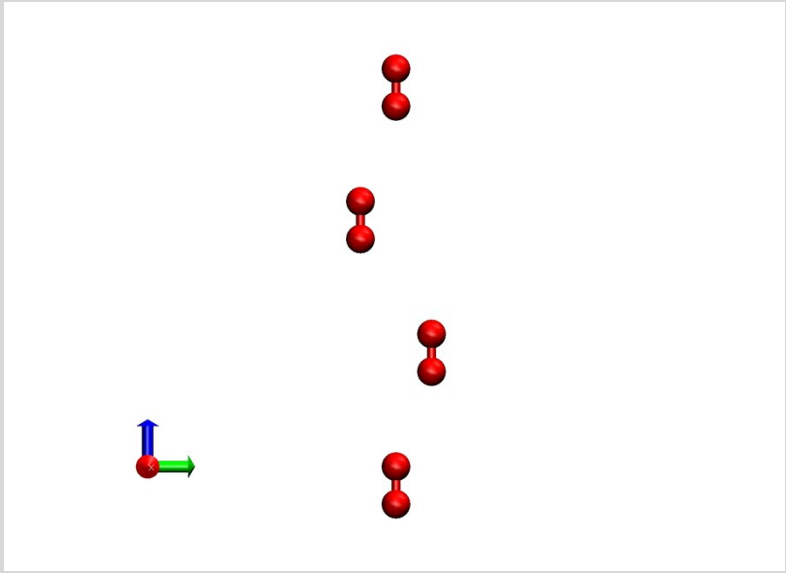

Movie S5.5: Movie of the same deformation simulation as in Movie S5.1 with the [$10\bar{1}$] (*x*-axis) pointing out of the page. Periodic images of the reference structure are removed in *y* but kept in the *x* direction, and the focus is only on a few molecules. As the system shears, the molecules tilt sideways indicating a change in the azimuth angle, θ.

S6: Finding the Angle between Crystallographic Planes in a Rhombohedral Cell

The equation to determine the angle between crystallographic planes for a rhombohedral system can be found in Table 4 of reference [6]. However, it should be noted that the published equation has missing brackets and should read:

$$\cos\theta_{12} = \frac{d_1 d_2\left[(h_1h_2 + k_1k_2 + l_1l_2)\sin^2\alpha + \{h_1(k_2 + l_2) + k_1(h_2 + l_2) + l_1(h_2 + k_2)\}(\cos^2\alpha - \cos\alpha)\right.}{a^2(1 - 3\cos^2\alpha + 2\cos^3\alpha)}$$

S7: Rotational Twinning Movies of β-oxygen

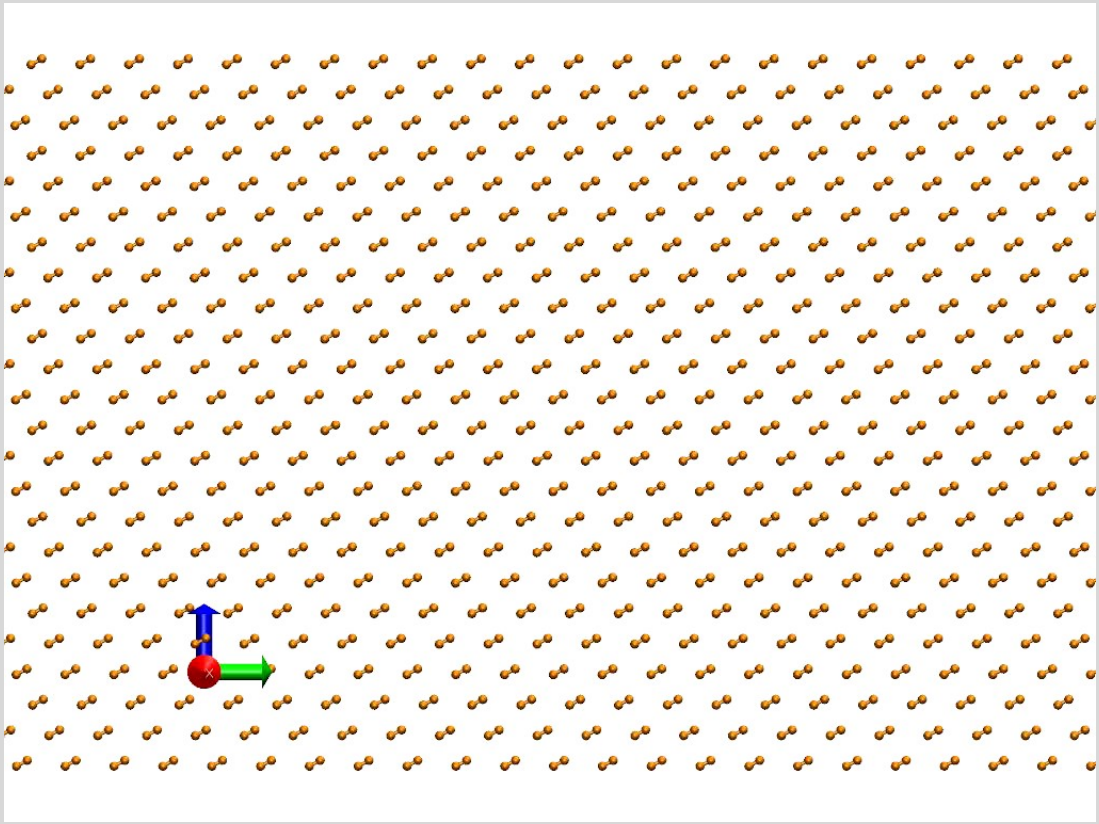

Movie S7.1: RBSM deformation movie of the 12 layer system sheared along (110)[$\bar{0}01$]. The top-most six molecules belong to region three and the bottom-most six molecules belong to region two (the other five molecules are not shown). The [$\bar{0}01$] direction is aligned along -*y* (anti-parallel to the green arrow) and [$\bar{1}\bar{1}1$] aligned along *z* (blue reference arrow). Rotational twinning is clearly observed as molecules rotate due to strain.

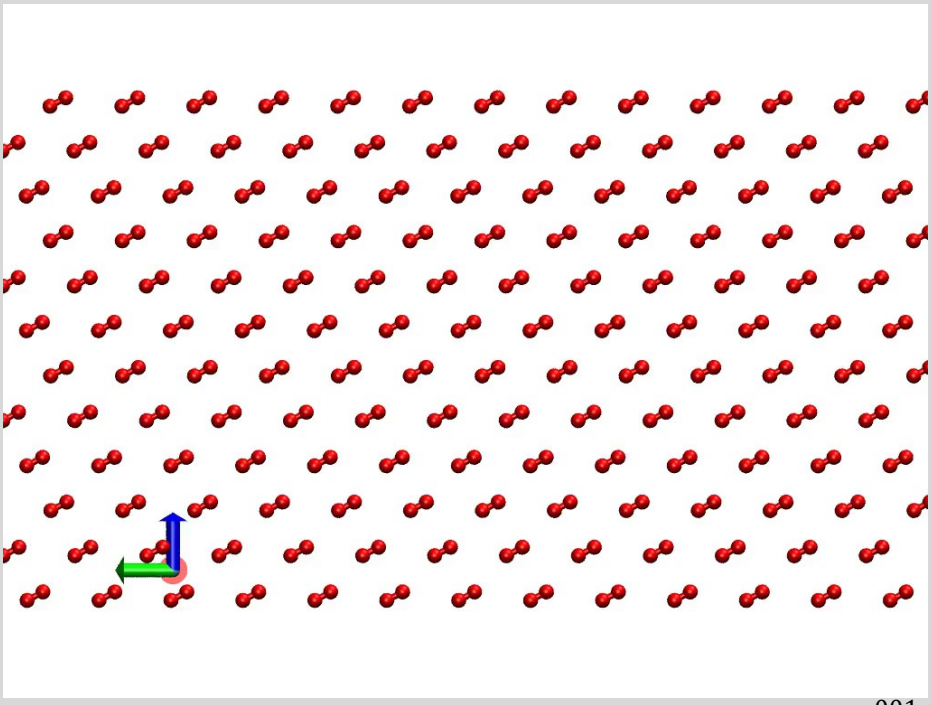

Movie S7.2: TBSM deformation twinning movie of the 12 layer system sheared along (110)[$\bar{1}$$\bar{1}$0]. The [$\bar{1}$$\bar{1}$0] direction lies in the *yz* plane. Twinning manifests itself through the rotation of molecules throughout the supercell.

S8: Characterisation of Slip Systems in Anthracene by TEM

S8.1 Experimental

Anthracene (Aldrich, AR grade) was purified by repeated sublimation in the dark to remove photochemically induced impurities (*e.g.* dipara-anthracene and anthraquinone). The purified anthracene was dissolved in xylene (Aldrich, AR grade) and a thin layer of the solution (approximately 10^{-3} M) was poured onto the surface of distilled water and allowed to evaporate at room temperature under controlled conditions in the dark. The resulting plate-like crystals (typically 200 nm thick with lateral dimensions up to mm) were lifted onto 400 mesh copper TEM grids, and any attached water was allowed to evaporate before the anthracene crystals were examined in the TEM.

A Siemens Elmiskop 1 TEM was used at the Department of Metallurgy, University of Oxford, operating at 100 kV, with a custom-made, double-tilt liquid helium-cooled stage, giving a sample temperature of approximately 10K [7]. The low temperature is necessary to reduce the radiation damage caused by the electron beam.

S8.2 Results

In Figure S8.2.1, the dislocation labelled AB is not visible in the dark field image taken using the (20$\bar{2}$) reflection, from which it is deduced that the Burgers vector is [010]. The dislocations are tens of microns in length; as the crystals are less than 400 nm thick, the dislocations must lie on the (001) plane; hence the slip system is (001)[010].

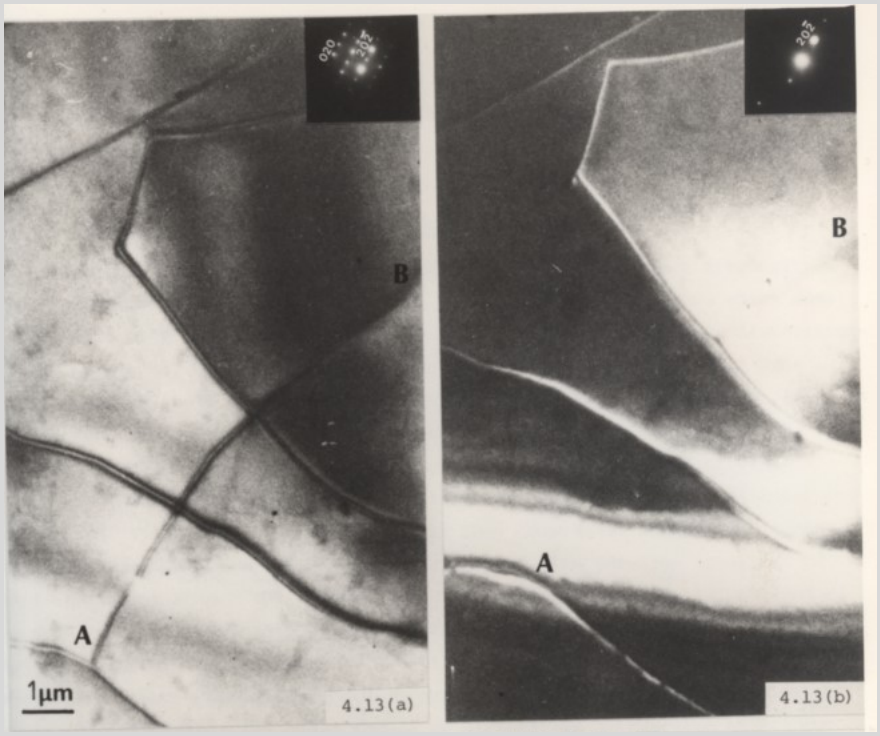

Figure S8.2.1: Example of using TEM bright and dark field imaging to identify the slip system based on an observed dislocation.

In the current study, it was not possible to determine the magnitude of the Burgers vectors by TEM (*e.g.*, distinguish between (001)[110] and (001) ½[110]), just their direction. By comparing the direction of the dislocations with their crystallographic orientations, edge, screw, and mixed dislocation types were identified.

TEM also showed interactions between dislocations, for example between (001){010] and (001)[100] dislocations, and the following reaction is hypothesised:

(001)[010] + (001)[100] →(001)[110]

S9: RBSM and TBSM Molecular Rotations in Anthracene (001)[010]

Figure 15 in the main text shows the strain energy as a function of strain for shearing anthracene surface cell along (001)[010]. As the surface cell is strained, the normalised strain energy increases due to the smooth movement of the centre of mass and smooth rotations of molecules until a first micro-slip event happens at a strain of about 0.1, which determines the slip barrier. This miniscule event on the normalised strain energy scale corresponds to a jump in the rotation of anthracene molecules and the differential displacement, followed by additional non-smooth rotations and centre of mass motion as the energy increases until region 3 slips with respect to region 1; angular distortions will be discussed below. The slip cycle is repeated between regions 3 and 1; this is illustrated in Movie S9.5. The ten and sixteen layer systems in Figure 15 show a particular response such that the first barrier represents a sudden jump in the centre of mass motion and rotations, while the second barrier corresponds to slip between regions 3 and 1, and simulations with even more layers show that the point of slip seems to diverge.

However, the observation that the second barrier 0.2346 of the sixteen layer simulation is greater than the same quantity (0.2307) for the ten layer simulation should not be interpreted as divergence, but rather as the system acquiring the necessary energy to adjust the additional intermolecular distortions due to the size of the system to trigger the slip state. These results imply that molecular rotations play a critical role in the slip of anthracene, especially due to the presence of two anthracene molecules per unit cell. Thus, a surface or a supercell has these two distinct molecules per layer (arbitrarily denoted as A and B); we plot the rotations of these two anthracene molecules in Figure S9.1, which shows a smooth change of the angular rotations of anthracene molecules between zero strain and the first micro-slip event at about 0.1 strain.

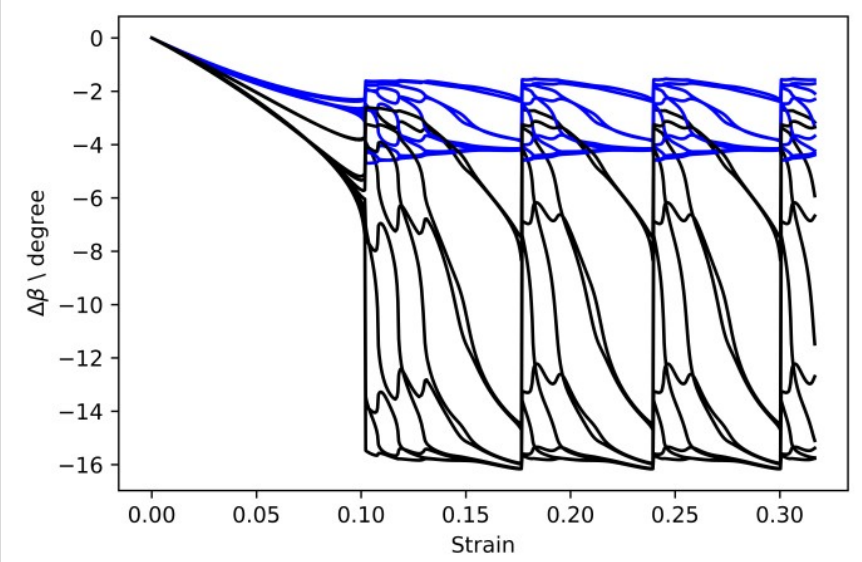

Figure S9.1: Change in β (rotation about y-axis) as a function of all the molecules' strain in region 1 for the ten layer case of anthracene sheared via RBSM in (001)[010]. We differentiate two rotation groups (blue and black) where black represents A molecules whose centre of mass is closest to the origin of the anthracene unit cell, while blue represents B molecules, whose centre of mass is closest to the centre of the unit cell.

Beyond the micro-slip event, the change in the angular distortions is very complicated and divides into two groups denoted by black and blue curves, where each curve corresponds to either molecule A or B in the anthracene surface cell. Figures S9.2 and S9.3 show these angular distortions in more detail.

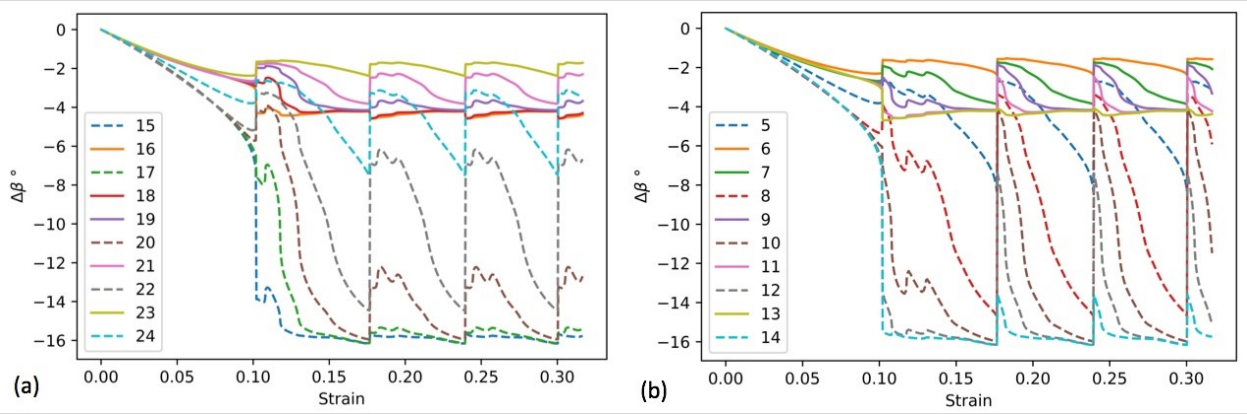

Figure S9.2: Change in the β angle as a function of strain for RBSM shearing in (001)[010]. (a) plots the angles of molecules numbers 15 to 24 in region one, while (b) plots the same for molecules 5 to 14. The dashed and solid lines correspond to the two different arbitrary types of anthracene molecules, i.e. A and B.

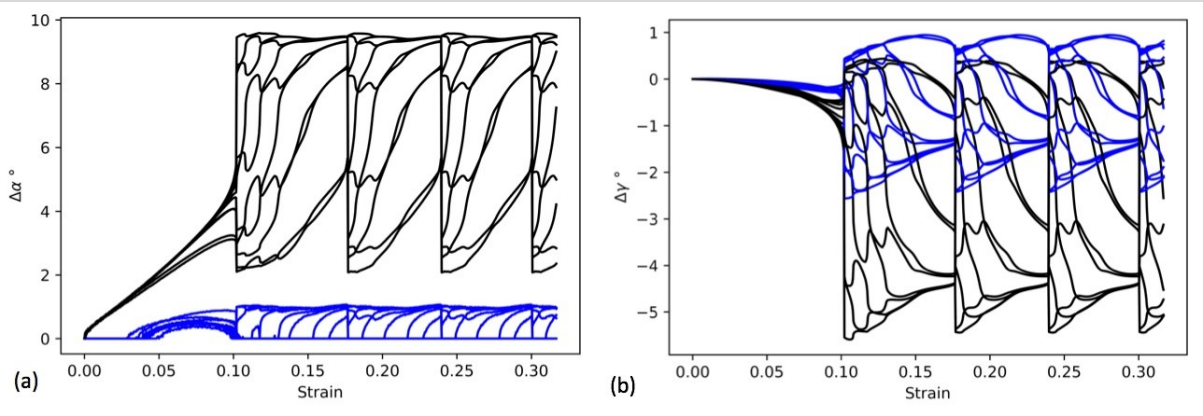

Figure S9.3: Change in (a) α, and (b) γ, as a function of strain for RBSM shearing in (001)[010] for anthracene. The black and blue curves correspond to the rotations of molecules of types A and B, respectively.

The highest change in the molecular distortion is found to occur near the mid-section of region 1 for type A molecules and starts decreasing as the rigid blocks are approached. Similar smooth and non-smooth angular rotations of molecules have been observed for the other two rotations, but to a lesser extent. Our analysis shows that shearing the (001)[010] direction in anthracene causes 3D rotation of molecules, the highest near the mid-section of region 1. At the same time, when the saturation limit is reached within the structure, the system slips between regions 3 and 1. Movie S9.5 shows RBSM shearing of the (001)[010] in anthracene, molecular rotations, movement of the molecules, and slip events.

Figure S9.4 shows the molecular rotations of anthracene as a function of strain for TBSM shearing (001)[010]. Because of the interchange of axes, α, β, and γ in RBSM correspond to α, γ, and β in TBSM. By comparing Figure S9.4 with Figures S9.1 and S9.3, angular distortions in TBSM are homogeneous across all molecules, which is not the case for those in RBSM. Moreover, the direction of rotations and their maximum absolute values are similar between both methods, except for γ and β in RBSM and TBSM, respectively, where TBSM leads to about three times the molecular distortion found for RBSM. These results imply that shear-induced rotational distortion in molecular crystals involves the three Cartesian components, which complicates the analysis of the deformation space.

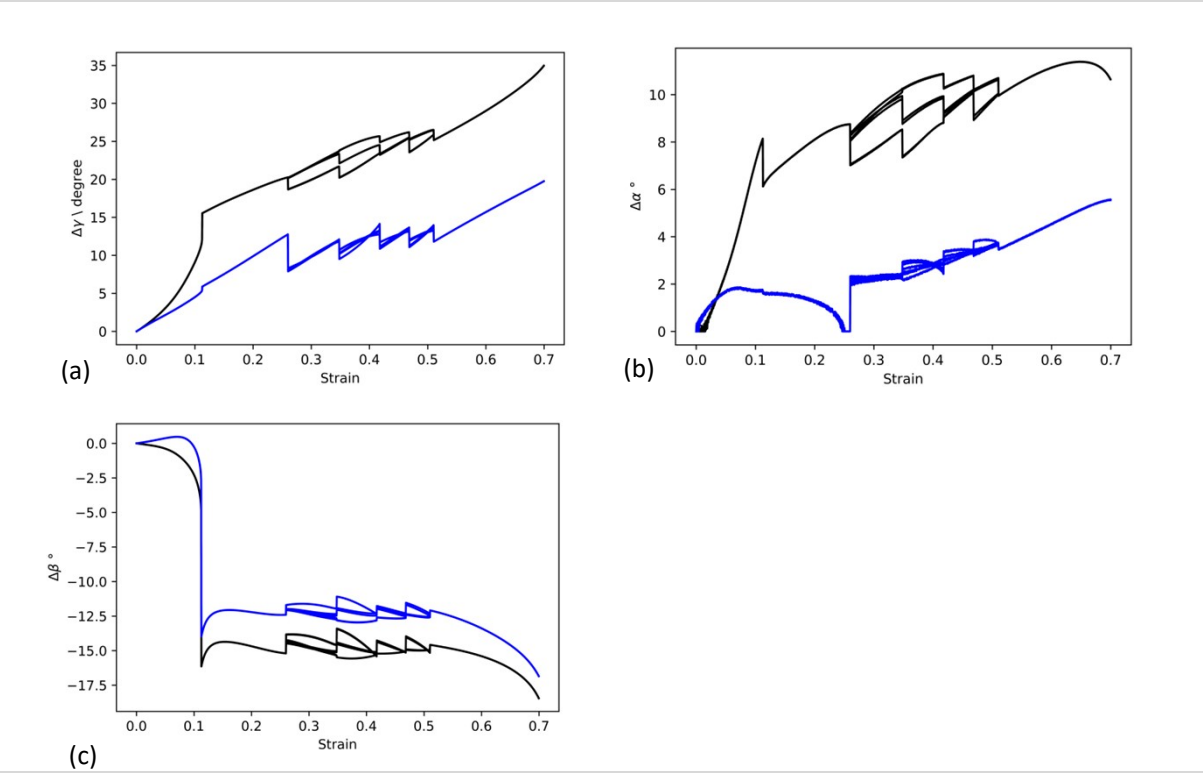

Figure S9.4: Change in γ (rotation about x, where the x-direction in this TBSM simulation is congruent to the y-direction in RBSM, *i.e.*, the x and y axes were interchanged) in (a), α in (b), and γ in (c), as a function of strain for TBSM shearing of the (001)[010]. The supercell has six layers, *i.e.*, twelve molecules. Black represents A molecules whose centre of mass is closest to the origin of anthracene unit cell, while blue represents B molecules, whose centre of mass is closest to the centre of the unit cell.

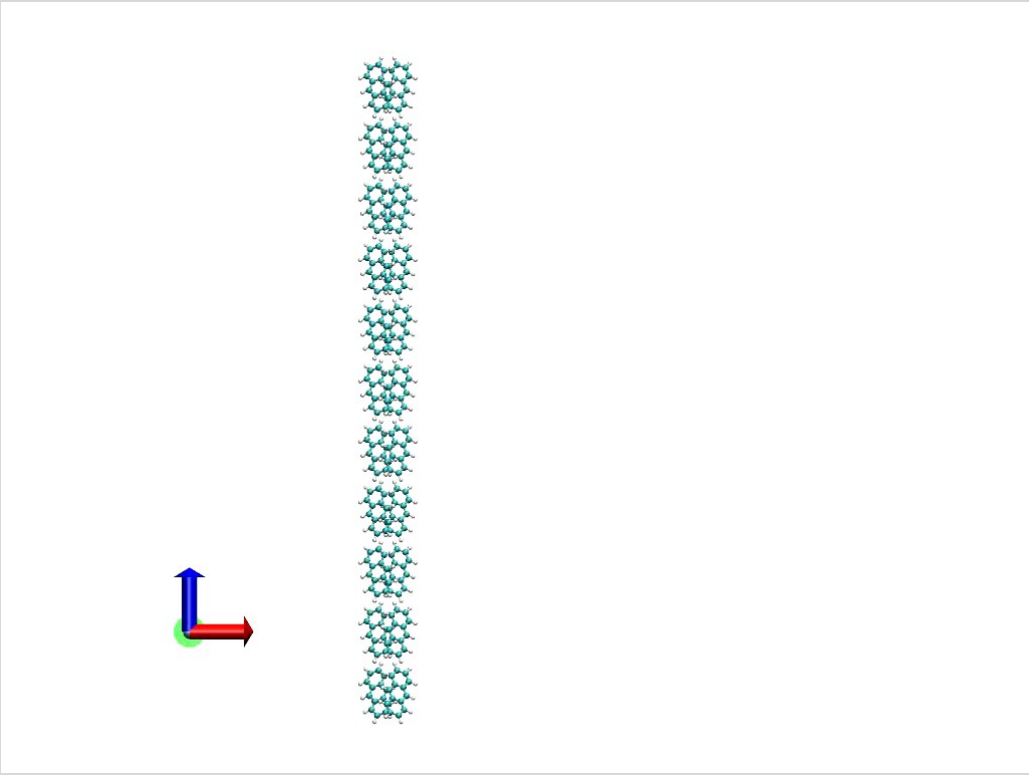

Movie S9.5: Trajectory of the 10 layer surface cell deformed by RBSM shearing in (001)[010]. The top layer belongs to region three and bottom-most layer is the last one in region one, while all other molecules are hidden.

S10: RBSM Rotational Twinning in Anthracene (001)[110]

Rotational twinning was introduced in the case of diatomic oxygen in terms of geometric distortion and the twinning interfacial energy. Anthracene molecules are planar and thus possess three distinct rotations about the axes of the molecule, while two were sufficient for diatomic oxygen. The movie in S10.1 shows deformation twinning in (001)[110] for a ten layer system; molecules in regions three and two are not shown.

The main text reports the change of γ as a function of strain when investigating rotational twinning in anthracene. Figure S10.2 reports the change in α and β as a function of strain indicating that rotational twinning in anthracene involves rotating about three axes.

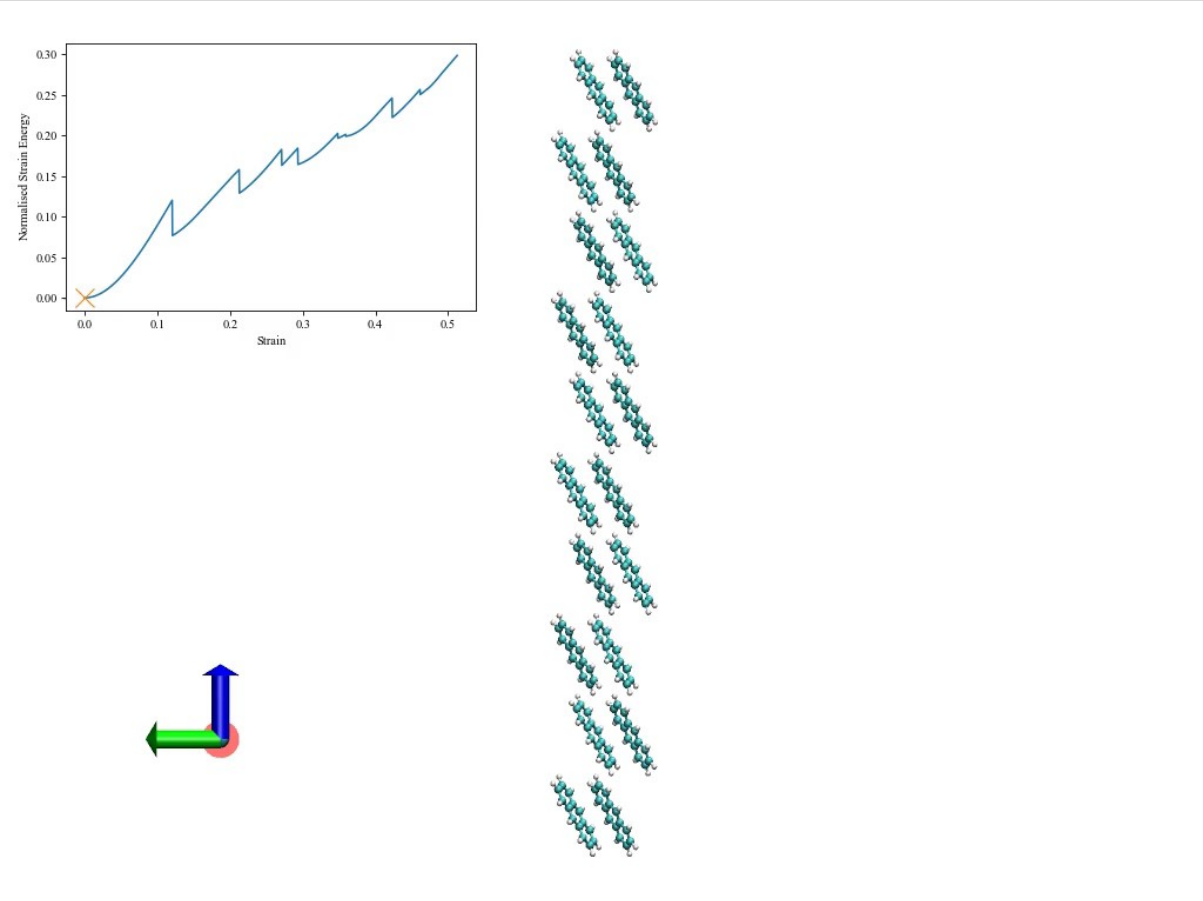

Movie S10.1: The trajectory of a 10 layer surface cell of anthracene is sheared via RBSM along (001)[110]. The normalised strain energy plot is also appended to the movie with the cross denoting the point on the graph corresponding to the frame currently being visualised.

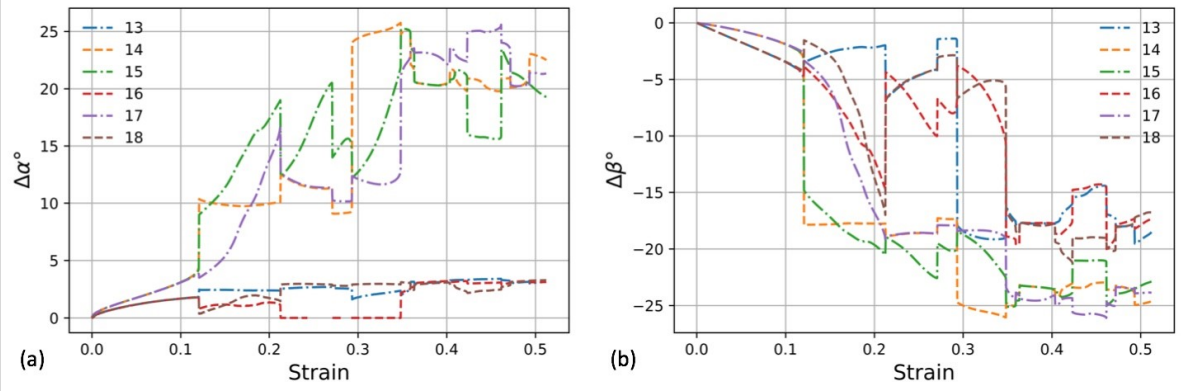

Figure S10.2: The change in (a) α, and (b) β as a function of strain for selected molecules in region one, for the case of a 10 layer anthracene surface cell sheared via RBSM along (010)[110].

S11: RBSM Rotational Twinning in Anthracene (001)[100]

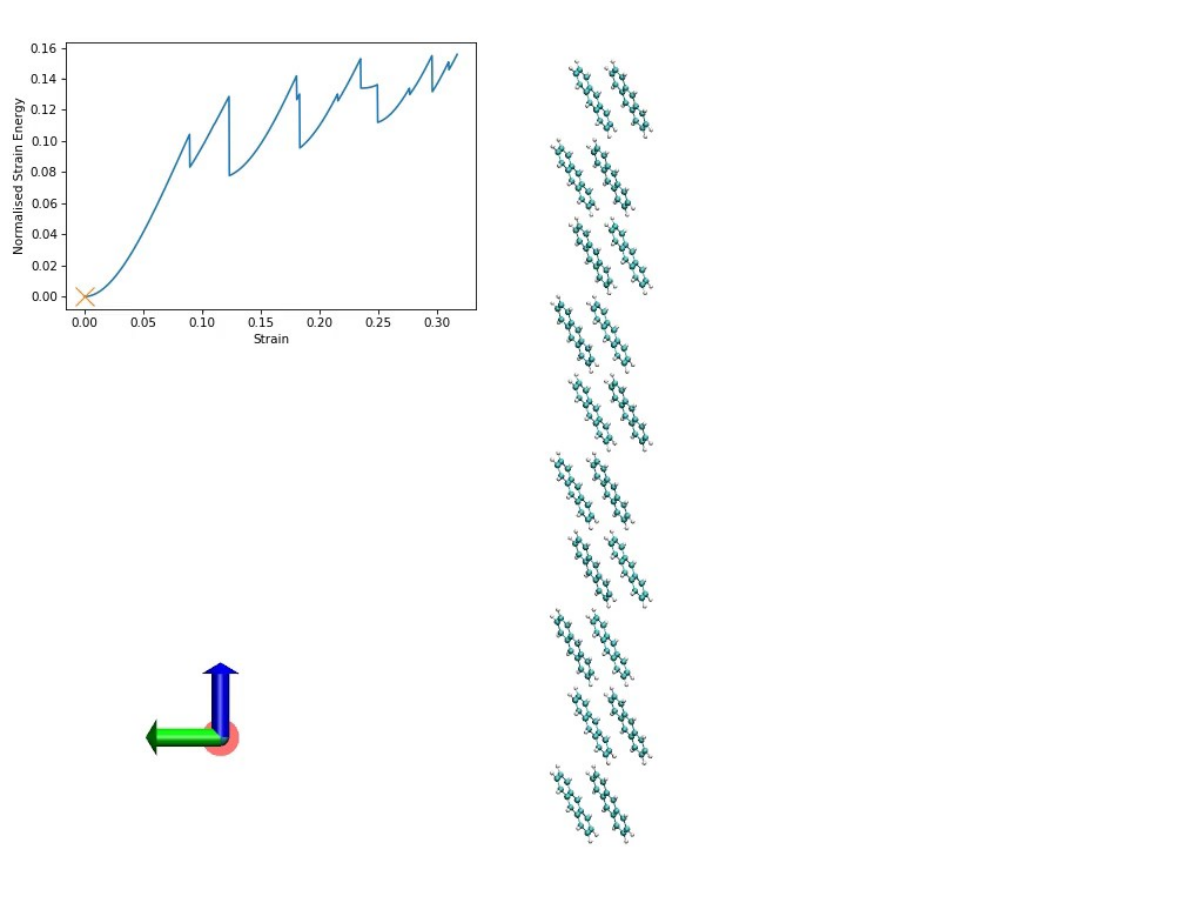

Movie S11.1: The trajectory of a 10 layer surface cell of anthracene is sheared via RBSM along (001)[100]. The normalised strain energy plot is also appended to the movie with the cross denoting the point on the curve corresponding to the frame currently being visualised.

The Movie S11.1 shows the trajectory of rotational twinning deformation of anthracene sheared along (001)[100] via RBSM. The normalised strain energy plot is embedded in the movie. There are several subsequent slip barriers with an increasing trend as a function of strain indicating that twinning is difficult to grow in anthracene (001)[100].

Figure S11.2 describes some aspects of deformation twinning in the (001)[100], where (a) reports the strain and re-optimisation surface energies. Figure S11.2 (b) shows that deformation twinning involves the rotation of molecules by $\gamma \approx 60°$ about the x-axis, and rotations about the y and z, as shown in Figures S11.2 (c) and (d) which are different compared to the same rotations for rotational twinning in (001)[110]. The results in Figure S11.2 imply that rotational twinning deformation in (001)[100] has similar features to rotational twinning deformation in (001)[110].

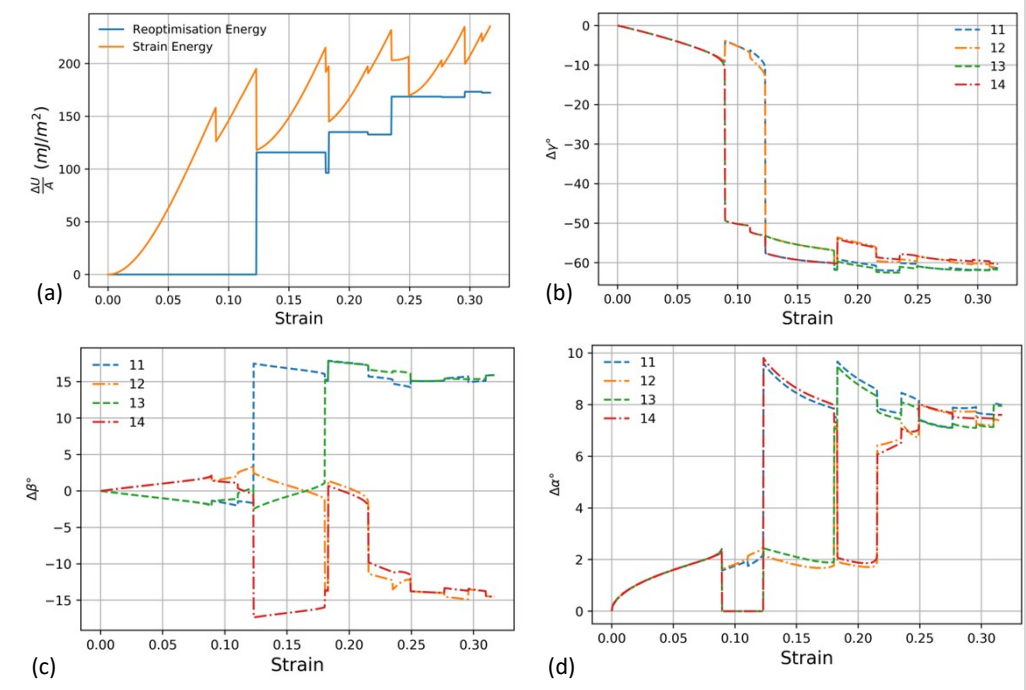

Figure S11.2: (a) Shows the strain and re-optimisation surface energies as a function of strain, while (b), (c), and (d) show the change in γ, β, α, respectively, as a function of strain for the important molecules indexed in the legend.

S12: Mechanically Induced Polymorphic Transitions in Anthracene

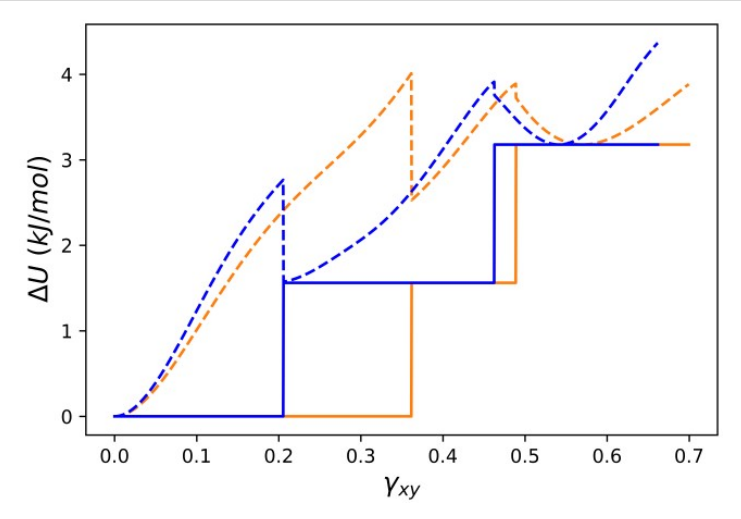

Figure S12.1: TBSM relative strain energies per molecule (dashed lines) with respect to the reference structure, and the relative re-optimised strain energy per molecule (solid lines), as a function of strain. Orange traces represent the results for (001)[100], while the blue ones represent the same for (001)[110].

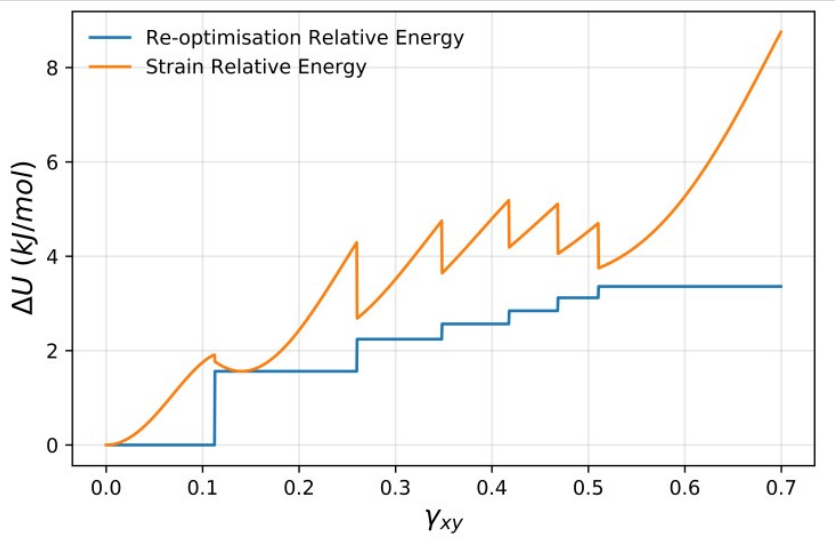

Figure S12.2: Strain and re-optimisation relative energies per molecule as a function of strain for TBSM shearing along (001)[010].

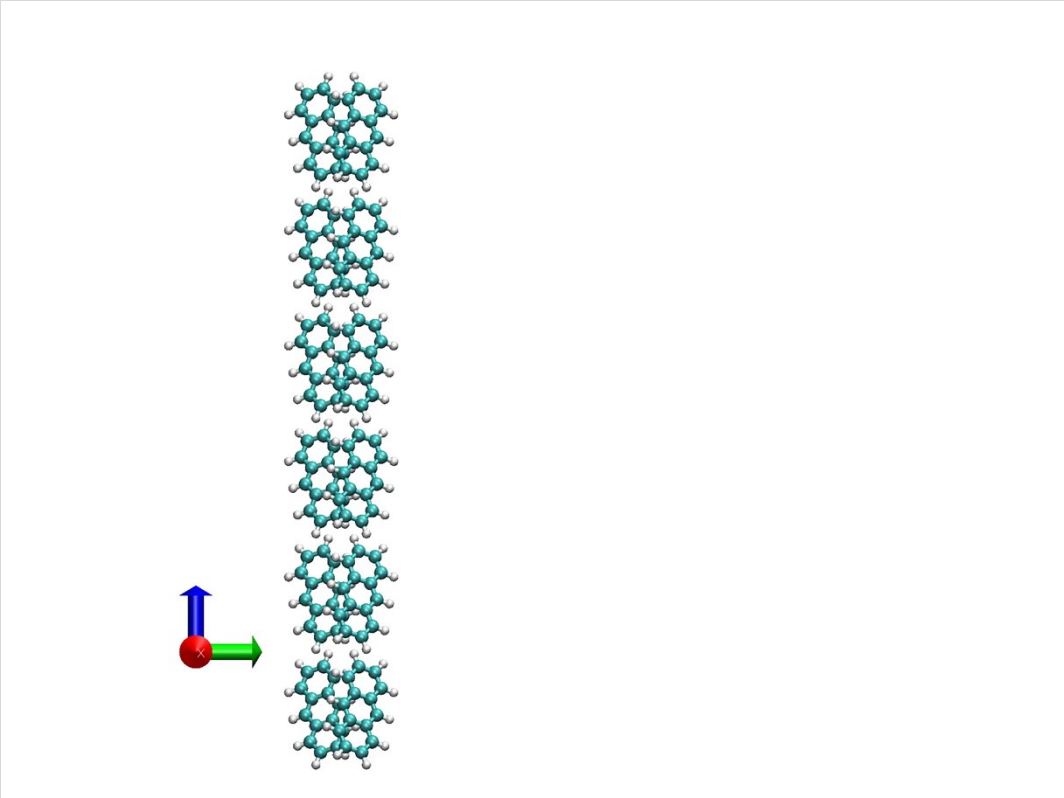

Movie S12.3: The deformation trajectory of a 6 layer supercell sheared using TBSM along the (001)[010] system. The polymorphic transition events and their sequence are observed across the layers.

S13: Higher Accuracy Quantum Mechanical Methods

For anthracene, some structures need to be examined with a higher accuracy level of theory. Thus, we used dispersion-corrected density functional theory (DFT-D) employing the PBE functional [8] with Neumann-Perrin (NP) dispersion [9] to perform these calculations. DFT-D

calculations in VASP 5.4.1 used a plane wave cut-off energy of 520 eV with the default PAW pseudopotentials. All lattice optimisations were converged to at least 0.007 Å for maximum atomic displacements, 0.0005 kcal mol^{-1}/atom for energy changes, 2 kcal mol^{-1}/Å for maximum atomic forces, and 4.0 kbar for the maximum cell stress.

S14: RMSD15 Analysis of the Virtual Polymorphs

RMSD15 analysis was conducted as per the main text. Table S14.1 reports the RMSD values for the overlay of 15 molecules for polymorphs Po1, Po2, and Po3, with respect to the reference experimental structure Po0, using both DFT and FF.

Polymorph	Po1	Po2	Po3
RMSD FF (Å)	0.541	0.966	0.492
RMSD DFT (Å)	0.519	1.657	0.424
Overlaid Molecules FF / 15	9	7	7
Overlaid Molecules DFT /15	9	6	7

Table S14.1: RMSD15 analysis for the overlay of the 15 molecules of the virtual polymorphs Po1, Po2, and Po3, with respect to the experimental structure Po0.

The above analysis clearly indicates that all the polymorphs are unique since the number of overlaid molecules is below 15.

To verify that the virtual polymorphs reported in this paper are unique with respect to the structures present in the Cambridge Crystallographic Database, we compared the lattice parameters, where possible, or performed RMSD15 analysis. Because the virtual polymorphs have triclinic structures, it is non-trivial to compare them even to any other reported triclinic polymorph as no single unique unit cell describes the system. Our analysis has shown that the experimental structure is different compared to the virtual polymorph. Hence, all the structures in the Cambridge Crystallographic Database that match our experimental structure cannot match the virtual polymorphs. The table below compares the experimental structure (the reference structure used in our calculations optimised using DFT) to 15 Cambridge Crystallographic Database structures.

CCDB	*a* (Å)	*b* (Å)	*c* (Å)	alpha (°)	beta (°)	gamma (°)	Space group
ANTCEN	8.562	6.038	11.184	90	124.7	90	P 21/a
Exp-ANTCEN	0.6	1.0	0.0	0.0	0.1	0.0	P 21/a - P 21/a
ANTCEN01	8.4144	5.9903	11.0953	90	125.293	90	P 21/a
Exp-ANTCEN01	-1.2	0.2	-0.8	0.0	0.6	0.0	P 21/a - P 21/a
ANTCEN02	8.4144	5.9903	11.0953	90	125.293	90	P 21/a
Exp-ANTCEN02	-1.2	0.2	-0.8	0.0	0.6	0.0	P 21/a - P 21/a
ANTCEN03	8.561	6.036	11.163	90	124.7	90	P 21/a
Exp-ANTCEN03	0.6	1.0	-0.2	0.0	0.1	0.0	P 21/a - P 21/a
ANTCEN04	8.561	6.036	11.163	90	124.7	90	P 21/a
Exp-ANTCEN04	0.6	1.0	-0.2	0.0	0.1	0.0	P 21/a - P 21/a

ANTCEN07	11.174	8.554	6.016	90	90	124.6	P 1 1 21/b
Exp-ANTCEN07	-0.1	0.5	0.7	0.0	0.0	0.0	P 1 1 21/b - P 21/a
ANTCEN08	11.092	8.407	6.006	90	90	125.31	P 1 1 21/b
Exp-ANTCEN08	-0.9	-1.3	0.5	0.0	0.0	0.6	P 1 1 21/b - P 21/a
ANTCEN09	8.4144	5.9903	11.0953	90	125.293	90	P 21/a
Exp-ANTCEN09	-1.2	0.2	-0.8	0.0	0.6	0.0	P 21/a - P 21/a
ANTCEN10	8.4414	5.9958	11.1123	90	125.175	90	P 21/a
Exp-ANTCEN10	-0.9	0.3	-0.7	0.0	0.5	0.0	P 21/a - P 21/a
ANTCEN11	8.4673	5.9994	11.1244	90	125.056	90	P 21/a
Exp-ANTCEN11	-0.5	0.4	-0.6	0.0	0.4	0.0	P 21/a - P 21/a
ANTCEN12	8.4959	6.0033	11.1407	90	124.07	90	P 21/a
Exp-ANTCEN12	-0.2	0.5	-0.4	0.0	-0.4	0.0	P 21/a - P 21/a
ANTCEN13	8.5254	6.0088	11.1548	90	124.757	90	P 21/a
Exp-ANTCEN13	0.1	0.5	-0.3	0.0	0.1	0.0	P 21/a - P 21/a
ANTCEN14	8.5526	6.0158	11.172	90	124.596	90	P 21/a
Exp-ANTCEN14	0.5	0.7	-0.1	0.0	0.0	0.0	P 21/a - P 21/a
ANTCEN15	8.542	6.016	11.163	90	124.59	90	P 21/a
Exp-ANTCEN15	0.3	0.7	-0.2	0.0	0.0	0.0	P 21/a - P 21/a
ANTCEN16	8.37	6	11.12	90	125.4	90	P 21/a
Exp-ANTCEN16	-1.7	0.4	-0.6	0.0	0.6	0.0	P 21/a - P 21/a

Table S14.2: Lattice parameters comparison between the experimental (reference) structure used here and other structures from the Cambridge Crystallographic Database. The green rows report the percentage error for the values in the previous line.

Table S14.2 shows that the maximum error in comparing the lattice parameters is 1.7 % which confirms that all these structures are crystallographically equivalent to the reference structure used here. For the remaining structures, except ANTCEN18, RMSD15 analysis was performed and found that 15 molecules were able to be overlaid indicating that all these structures are crystallographically equivalent to the reference structure, see the RMS reported in the table below.

CCDC	RMSD (Å)
ANTCEN17	0.099
ANTCEN19	0.046
ANTCEN20	0.106
ANTCEN21	0.096
ANTCEN22	0.115
ANTCEN23	0.096
ANTCEN24	0.089
ANTCEN25	0.097
ANTCEN26	0.042

Table S14.3: RMSD15 analysis of structures from the Cambridge Crystallographic Database versus the reference structure used in this work.

References:

1. Kobashi, K., M.L. Klein, and V. Chandrasekharan, *Lattice dynamics in solid oxygen.* The Journal of Chemical Physics, 1979. **71**(2): p. 843-849.
2. Mei, J., J.W. Davenport, and G.W. Fernando, *Analytic embedded-atom potentials for fcc metals: Application to liquid and solid copper.* Physical Review B, 1991. **43**(6): p. 4653-4658.
3. Cahill, J.E. and G.E. Leroi, *Raman Studies of Molecular Motion in Condensed Oxygen.* The Journal of Chemical Physics, 1969. **51**(1): p. 97-104.
4. Barrett, C.S. and L. Meyer, *Molecular Packing, Defects, and Transformations in Solid Oxygen.* Physical Review, 1967. **160**(3): p. 694-697.
5. Fleming, S. and A. Rohl, *GDIS: a visualization program for molecular and periodic systems*, in *Zeitschrift für Kristallographie - Crystalline Materials*. 2005. p. 580.
6. Tannous, C., *Crystal structure, x-ray diffraction and oblique geometry.* European Journal of Physics, 2019. **41**(1): p. 015501.
7. Hobbs, L.W., A.E. Hughes, and G. Chassagne, *Direct observation of alkali metal colloids in alkali halide crystals.* Nature, 1974. **252**(5482): p. 383-385.
8. Perdew, J.P., K. Burke, and M. Ernzerhof, *Generalized Gradient Approximation Made Simple.* Physical Review Letters, 1996. **77**(18): p. 3865-3868.
9. Neumann, M.A. and M.-A. Perrin, *Energy Ranking of Molecular Crystals Using Density Functional Theory Calculations and an Empirical van der Waals Correction.* The Journal of Physical Chemistry B, 2005. **109**(32): p. 15531-15541.